THE ASTROPHYSICAL JOURNAL, 421:245–260, 1994 January 20

PENETRATION BELOW A CONVECTIVE ZONE

NEAL E. HURLBURT
Lockheed Solar and Astrophysics Laboratory, Organization 91-30, Building 252, 3251 Hanover Street, Palo Alto, CA 94304
JURI TOOMRE
Joint Institute for Laboratory Astrophysics[1] and Department of Astrophysical, Planetary, and Atmospheric Sciences, University of Colorado, Boulder, CO 80309-0440
JOSEP M. MASSAGUER
Department Fisica Aplicada, Universidad Politecnica de Barcelona, Jorge Girona Salgado 31, Barcelona 08034, Spain
AND
JEAN-PAUL ZAHN
DASGAL, Observatoire de Meudon, 92195 Meudon Cedex, France,[1] and Astronomy Department, Columbia University, New York, NY 10027
Received 1993 April 1; accepted 1993 August 2

ABSTRACT

Two-dimensional numerical simulations are used to investigate how fully compressible nonlinear convection penetrates into a stably stratified zone beneath a stellar convection zone. Estimates are obtained of the extent of penetration as the relative stability S of the stable to the unstable zone is varied over a broad range. The model deals with a perfect gas possessing a constant dynamic viscosity. The computational domain is divided into regions of initially stable and unstable polytropic stratification by varying the thermal conductivity with depth. Effects of compressibility are accentuated by considering cases where the mean density ratio across the unstable zone is initially 6, and as much as 114 across the entire domain. The dynamics is dominated by downward-directed plumes which can extend far into the stable material and which can lead to the excitation of a broad spectrum of internal gravity waves in the lower stable zone. The convection is highly time dependent, with the close coupling between the lateral swaying of the plumes and the internal gravity waves they generate serving to modulate the strength of the convection. The depth of penetration Δ, determined by the position where the time-averaged kinetic flux has its first zero in the stable layer, is controlled by a balance between the kinetic energy carried into the stable layer by the plumes and the buoyancy braking they experience there. A passive scalar is introduced into the unstable layer to evaluate the transport of chemical species downward. Such a tracer is effectively mixed within a few convective overturning times down to a depth of Δ within the stable layer. Analytical estimates based on simple scaling laws are used to interpret the variation of Δ with S, showing that it first involves an interval of adiabatic penetration if the local Peclet number of the convection exceeds unity, followed by a further thermal adjustment layer, the depths of each interval scaling in turn as S^{-1} and $S^{-1/4}$. These estimates are in accord with the penetration results from the simulations.

Subject headings: convection — hydrodynamics — methods: numerical — stars: interiors

1. INTRODUCTION

Thermal convection can be effective at redistributing energy, angular momentum and chemical elements in stellar interiors. Mixing-length approaches have provided the primary means for describing the heat transport achieved by such convection in stars and thus are one of the mainstays of stellar structure and evolution theory. These mixing-length treatments are often lamented, for the assumptions upon which they are based are rather simplistic and are difficult to confirm experimentally. Yet such local mixing-length descriptions of convection prevail because of the ease with which they can be implemented, and it may well be that they treat some aspects of the mixing achieved within convection zones quite adequately. However, such approaches have real problems in treating motions that penetrate into the stably stratified layers which surround convection zones. Efforts at rendering local theories nonlocal in order to describe such penetrative convection have led to uncertain results, as discussed in turn by Renzini (1987) and Zahn (1991), for the predictions about the extent of penetration vary widely depending upon the assumptions made. The nonlocal mixing-length models typically determine the convective velocities from an integral of the stratification with depth, with work done by buoyancy leading to changes in the kinetic energy of a fluid element. Though such nonlocal approaches permit motions to extend well beyond the unstable zone, the extent of penetration depends sensitively on the imposed integral scale (or mixing length) with depth, and attempts to calibrate that integral scale have yielded diverse conclusions. Further, the role which compressibility plays in the highly nonlinear flows of stellar convection is still unclear and deserves particular attention.

Numerical simulations of convection have been pursued as an alternative means of trying to assess the properties of vigorous compressible convection in stellar settings. Early nonlinear studies were carried out within the anelastic approximation in which the dynamical equations are filtered to remove effects of sound waves, and with the further assumption that the horizontal structure of the convection could be expressed as a Galerkin expansion involving a truncated set of horizontal planforms or modes (Latour et al. 1976). Such anelastic modal equations in their simplest form, involving only a single mode, such as a hexagon in the horizontal but having excellent resolution in the vertical, were used to study compressible convection in the entire outer envelope of A-type stars (Toomre et

[1] Postal address.

al. 1976; Nelson 1980; Toomre 1980; Latour, Toomre, & Zahn 1981). Using realistic equations of state and opacities, these modal studies revealed that cellular flows of large horizontal scale, driven principally in the lower helium convection zone, would penetrate substantially above and below that region, leading to dynamical coupling of the two zones of instability in A stars, contrary to what had been inferred from mixing-length models. Such penetrative convection serves to preclude gravitational diffusive separation of elements in what was supposedly a quiescent stable region between the hydrogen and helium zones. Further, those modal solutions showed that the large-scale upward-directed flows were deflected sharply sideways by effects of major pressure fluctuations as they approached the hydrogen ionization zone, leading to strong shearing flows below the surface, with only a faint signature of the flows getting through into the atmosphere.

Anelastic modal equations were also used by Massaguer & Zahn (1980) to study nonlinear convection in a simpler unstable layer of a perfect gas initially stratified as a polytrope. They found that effects of compressibility could yield substantial buoyancy braking at the top of the layer due to pressure fluctuations modifying the density fluctuations (see also Glatzmaier & Gilman 1981). Further, the net pressure work extracted from compression and dilation of the fluid could well exceed the net work by buoyancy forces when the convection cells are of large horizontal extent and the density contrast across the layer, χ, is large. Massaguer et al. (1984) extended the anelastic modal studies to consider penetrative convection in three initially polytropic layers, finding that penetration into the lower stable layer by downward-directed plumes from the middle unstable one is considerably greater than that which is achieved in similar three-layer systems of Boussinesq fluid (Zahn, Toomre, & Latour 1982).

The fully compressible equations, admitting sound waves and with no restrictions on χ or the flow Mach number M, were first used in two-dimensional simulations of convection in unstable layers of a perfect gas extending over multiple scale heights and revealed in unstable layers of a perfect gas extending over multiple scale heights and revealed distinctive asymmetries between upward and downward flows (e.g., Graham 1975; Hurlburt 1983; Hurlburt, Toomre, & Massaguer 1984; Toomre, Hurlburt, & Massaguer 1984; Sofia & Chan 1984; Yamaguchi 1984, 1985; Porter et al. 1990; Cattaneo, Hurlburt, & Toomre 1990; Porter, Woodward, & Mei 1991; Xie & Toomre 1991, 1993; Porter & Woodward 1993a; see also Rast & Toomre 1993a, b for effects of ionization on the dynamics). The pressure fluctuations work in concert with temperature fluctuations to accentuate buoyancy driving in regions of descending motion but can even lead to buoyancy braking within the ascending motions, thereby yielding strong and narrow downward-directed plumes and weaker and broader upflows. Such asymmetries result in large downward-directed kinetic fluxes that partly counteract the upward-directed heat or enthalpy flux. The resulting flows are characterized by strong, narrow downward plumes surrounded by broad upflows, both extending over the entire depth of the convection zone. These fast-downflow plumes are realized in all the two-dimensional simulations of compressible convection, and thus one anticipates that such asymmetrical vertical flows could yield considerably greater penetration of convection into stable regions below an unstable zone rather than above it.

Two-dimensional compressible simulations of penetrative convection sought to make detailed contact with the earlier anelastic modal studies by adopting similar three-layer configurations (Hurlburt, Toomre, & Massaguer 1986, hereafter HTM), with the sequence of stable-unstable-stable layers achieved by specifying a varying thermal conductivity with depth. That study showed that the prominent downward-directed plumes could overshoot a substantial distance into the lower stable region, exciting a broad spectrum of internal gravity waves there, which in turn deflect the plumes laterally and yield a rich time dependence as they modulate the amplitude of the convection. In contrast, the extension of convective motions into the upper stable layer is far gentler, involving broad billowing flows accompanied by modest gravity wave excitation. Comparable behavior is reported from two-dimensional simulations by Porter et al. (1991) and Porter & Woodward (1993b) and further by Roxburgh & Simmons (1993) when employing a more general function of conductivity with temperature.

Since the penetrative properties are dominated by the presence of downflow plumes, it is essential to understand whether such up-down asymmetries arising from compressibility effects survive as the convection is allowed to be three-dimensional and to involve far more spatial degrees of freedom than allowed in the simpler modal treatments. The third spatial dimension permits vortex stretching mechanisms and associated shear instabilities which are precluded in two dimensions, and thereby provides one essential route to turbulence. Indeed, these instabilities might serve to disrupt the coherent downflow structures so evident in the two-dimensional simulations. Further, the enhanced degrees of freedom can yield flow topologies unattainable otherwise. Three-dimensional modeling of compressible convection necessary to answer such questions have gradually become available as the simulations have proceeded apace with advances in computer speed and memory. The three-dimensional compressible simulations fall broadly into two classes. In the first approach, the physics is simplified by using perfect gases (e.g., Graham 1977; Chan & Sofia 1986, 1989; Cattaneo, Hurlburt, & Toomre 1989; Malagoli, Cattaneo, & Brummell 1990; Hossain & Mullan 1990, 1991; Toomre et al. 1990; Cattaneo et al. 1991; Bogdan, Cattaneo, & Malagoli 1993; Porter & Woodward 1993a). In the second approach, granulation near the surface of the star is sought to be modeled, and thus realistic equations of state, opacities influenced by ionization effects, and radiative transfer processes are incorporated, along with outflow boundary conditions (e.g., Nordlund 1982, 1984, 1985 using anelastic equations; Stein & Nordlund 1989, 1991; Nordlund & Stein 1990; Rast et al. 1993). The two approaches have been complementary, with the simpler models used to search for generic properties of flow topologies and structures and transitions to turbulence and the more realistic models to see if such features survive in the presence of more intricate physics.

The three-dimensional simulations possessing adequate spatial resolution confirm that compressible convection involves distinctive asymmetries in its vertical flows. For moderate density contrasts χ of order 11, the convection near the top of a layer (where the scale height is small) is characterized by networks of narrow, cool sheets of fast downflow which surround isolated regions of broad, warm upflow. Thus the flow asymmetries seen in two-dimensional simulations, involving strong downflows and weaker upflows, are still very much in evidence. However, the topology of the cellular flows changes with depth: the sheets of downflow at cell peripheries near the top of the layer become concentrated into discrete

plumes at greater depths. These may coalesce into larger and larger plumes to form treelike structures (e.g., Stein & Nordlund 1989), or they may continue to descend into the layer, generating an increasingly turbulent flow as they go (e.g., Cattaneo et al. 1991). In the latter case, the coherent plume structures can coexist with intense small-scale turbulence, and there the plumes contribute little to the overall convective (enthalpy plus kinetic) energy transport, despite their vigor. Three-dimensional compressible simulations have also been used to study a few examples of penetrative convection within a two-layer configuration involving a stable layer positioned below an unstable one (Cattaneo & Malagoli 1993). The penetrating flows are again dominated by the discrete plumes interacting with the internal gravity waves they excite, leading to an extent of penetration of flows downward into the lower stable region which is roughly comparable to that obtained in the two-dimensional simulations by HTM for the same parameter values.

The emphasis upon plumes controlling the extent of penetration below a convection zone has also been employed in several promising analytical approaches. Schmitt, Rosner, & Bohn (1984) developed a model of stellar penetrative convection based upon isolated downward-directed plumes. With the assumption of self-similarity in the dynamics, they reduced the problem to a set of ordinary differential equations. Their numerical solutions of these equations determined that the depth of penetration scaled as $W^{3/2}$, where W is the velocity of the plume as it enters the stable region beneath the convection zone. More recently, Zahn (1991) developed a related simple model of penetration through the detailed application of scaling arguments to convection dominated by plumes. He posits that there are two distinct parts to the region of penetration in stellar interiors. The first is a region within the stable layer where the convection remains vigorous enough to modify the thermal stratification significantly, bringing it toward an adiabatic stratification. The second is a thermal boundary layer which forms to match the radiative flux deeper within the stable layer to that carried by the active convection at its base. The latter boundary layer will always be present, while the former will only be realized if the convection is reasonably efficient and possesses a sufficiently large Peclet number. Zahn assesses how these two elements will scale with the vigor of the convection and with the relative stability of the stable region, thereby providing estimates for the extent of penetration that may be achieved under varying conditions. In particular, Zahn explains why the depth of the adiabatic layer should scale as $W^{3/2}$, which was the numerical result of Schmitt et al. (1984).

We shall here turn to a suite of two-dimensional simulations of fully compressible penetrative convection, extending the studies of HTM to examine the effects of varying the relative stability S of the stable to the unstable layer, while dealing with greater density contrasts χ across the unstable layer to accentuate effects of compressibility. These direct simulations can then be used to judge the efficacy of the simpler analytical models and possibly serve to calibrate them, thereby providing a route by which they may be more reliably employed to estimate the extent of penetration achieved under realistic stellar conditions. We shall simplify the task by working with just a two-layer system, concentrating on the penetration achieved by the downward-directed plumes plunging into a region of stable stratification positioned below an unstable layer of convection.

The studies by HTM suggest that the presence of an upper stable layer is relatively benign if compared to that of the lower stable layer upon the overall convection, and thus we shall here confine attention to just a two-layer system. As in HTM, we shall impose upper and lower boundaries for the computational domain that are impermeable to flows and reflective to waves, rather than seeking to devise some form of open or transmitting boundaries, for we believe that the plumes and the associated penetration are insensitive to those boundary conditions, provided that the lower boundary is positioned sufficiently deep so as to not be impinged upon by the plumes. However, the detailed acoustic and gravity wave fields coupled to the convection are influenced by the character of those boundaries, and thus inferences about the associated wave field must be treated cautiously. We shall here concentrate on understanding how the dynamics of the plumes are influenced by the stability of that lower stable layer. To further simplify our surveys, we shall keep the properties of the unstable layer the same while varying the properties of the stable layer. These simulations will yield estimates of the extent of penetration achieved by such compressible convection. The results from our modeling can be used as test beds for scaling laws, such as those of Zahn (1991). These may then be applied more confidently to stellar parameter regimes which remain far away from that attainable by direct numerical simulation.

We believe that the two-dimensional simulations here which survey a range of parameters should be viewed as precursors to more proper three-dimensional modeling that should be carried out as computational resources permit, recognizing that it is only the latter that have the potential of describing fully turbulent processes with some modicum of accuracy. Nevertheless, recent progress with three-dimensional modeling of compressible convection suggests that the earlier two-dimensional approaches do capture many of the dominant features of such nonlinear dynamics, and this serves to encourage consideration of the computationally far less demanding simulations that are feasible when ignoring the third dimension. We shall pose the problem in § 2, discuss the results from surveys of solutions in § 3, then in § 4 develop scaling laws for a simple model of penetration and compare them with that achieved by the nonlinear simulations, and, finally, in § 5 assess what has been learned.

2. POSING THE PROBLEM

2.1. *The Model Atmosphere*

We shall consider penetrative convection in a compressible atmosphere consisting of two layers with differing initial stratifications. In keeping with the notation developed in HTM, the two layers are numbered sequentially in depth as 2 and 3 (the upper stable layer 1 is absent), with the upper layer 2 having an unstable stratification and the lower layer having a stable one. We control these stratifications by specifying the variation of the thermal conductivity $K(z)$ with depth z and assert that it is unaffected by the ensuing motions. The function $K(z)$ assumes differing constant values K_i within each layer and changes rapidly near the interface between them. Since the total energy flux F_T in a static state is independent of depth, the different thermal conductivities in each layer would produce different thermal gradients $\beta_i = F_T/K_i$ and hence control their stability to convection. For a perfect gas experiencing a constant gravitational acceleration, each initially quiescent layer has a polytropic stratification in which the temperature T, density ρ, and

pressure P can be expressed as

$$T = \beta_i(z - z_i) + T_i\,, \quad \rho = \rho_i\left(\frac{T}{T_i}\right)^{m_i}, \quad P = R_*\,\rho_i\,T_i\left(\frac{T}{T_i}\right)^{m_i+1}, \tag{2.1}$$

where m_i is the polytropic index, R_* is the gas constant, and $m_i + 1 = g/R_*\,\beta_i$. The top of each layer i is positioned at z_i, and the temperature T_i and density ρ_i are constants chosen to make T and ρ continuous in z; the chemical composition is taken as uniform. The top of both the unstable layer and of our computational domain is located at z_2, and the top of the lower stable layer is located at $z_3 \equiv z_2 + d$, where d is the depth of the unstable layer. Hence the density contrast across the unstable layer is $\chi_2 \equiv \rho_3/\rho_2$. The bottom of the computational domain is located at z_4.

For a fluid layer to be stable against convection, the Schwarzchild criterion requires the local polytropic index to be greater than the adiabatic polytropic index $m_a = 1/(\gamma - 1)$, where $\gamma = c_p/c_v$ is the ratio of the specific heats. As initial conditions, the polytropic index in the upper layer of our two-layer system is always taken less than m_a, whereas that in the lower layer is always greater. We find it useful to measure the relative stability S of these two layers by the positive parameter

$$S = -\frac{m_a - m_3}{m_a - m_2}\,. \tag{2.2}$$

We assume that the gas is monatomic, so that γ takes a constant value of 5/3. Therefore, stratifications with polytropic indices greater than 3/2 are convectively stable. We shall keep $m_2 = 1$ in the unstable layer and study the consequences of varying S by taking different values of $m_3 > 3/2$ in the stable layer.

We adopt the same scalings as in HTM. Namely, we scale length by d, fluid density by ρ_2, temperature by its difference across the unstable layer $\beta_2 d$, and time by $d/\sqrt{R_*\beta_2 d}$, which is related to the sound travel time across the unstable layer. The energy fluxes and rates of working will be scaled with respect to the total energy flux F_T as imposed on the lower boundary of the domain. All variables will be expressed in their dimensionless form hereafter.

2.2. *Equations*

We have solved the equations for fully compressible, nonlinear convection under the assumption that the motions are two-dimensional, with no variations or velocities in the second horizontal dimension. Hence our flows will depend upon time t, the horizontal coordinate $x \equiv x_1$, and the vertical coordinate $z \equiv x_2$, where z increases downward. The horizontal velocity in turn is $u \equiv u_1$, the vertical velocity is $w \equiv u_2$, and we assume $u_3 = 0$. Fully compressible motions are described by the equation for the conservation of mass

$$\frac{\partial \rho}{\partial t} + \frac{\partial}{\partial x_j}(\rho u_j) = 0\,, \tag{2.3}$$

the momentum equations

$$\frac{\partial}{\partial t}(\rho u_j) + \frac{\partial}{\partial x_k}(\rho u_j u_k) + \frac{\partial P}{\partial x_j} - \frac{\partial \tau_{jk}}{\partial x_k} - (m_2 + 1)\rho\,\delta_{j2} = 0\,, \tag{2.4}$$

where the last term is the buoyancy force, and the energy equation

$$\frac{\partial}{\partial t}\left\{\rho\left[\frac{T}{\gamma - 1} + \frac{1}{2}u_j u_j - (m_2 + 1)z\right]\right\} + \frac{\partial}{\partial x_k}\left\{\rho\left[\frac{\gamma T}{\gamma - 1} + \frac{1}{2}u_j u_j - (m_2 + 1)z\right]u_k - \frac{1}{Q}\frac{\partial T}{\partial x_k} - u_j\tau_{kj}\right\} = 0\,, \tag{2.5}$$

where the elements of the viscous stress tensor τ are

$$\tau_{jk} = \frac{\sigma_2}{Q}\left(\frac{\partial u_j}{\partial x_k} + \frac{\partial u_k}{\partial x_j} - \frac{2}{3}\delta_{jk}\frac{\partial u_l}{\partial x_l}\right), \tag{2.6}$$

with all indices $j, k, l = 1, 2$. These equations are supplemented by the equation of state for a perfect gas

$$P = \rho T\,. \tag{2.7}$$

Here we assume that the shear viscosity μ of the fluid is constant so that the Prandtl number in each layer, $\sigma_i = \mu c_p/K_i$, is constant. The ratio of the sound travel time to the thermal diffusion time at $z = z_2$ is

$$Q = \frac{(R_*\beta_2 d)^{1/2}\rho_2\,dc_p}{K_2}\,, \tag{2.8}$$

which is related to the midlayer Rayleigh number $\hat{R}$ by

$$\hat{R} = \frac{(m_2 + 1)(m_a - m_2)}{(m_a + 1)}\frac{Q^2}{\sigma_2}\frac{(z_2 + 1/2)^{2m_2 - 1}}{z_2^{2m_2}}\,. \tag{2.9}$$

We assume that the horizontal surfaces at z_2 and z_4 are impenetrable and stress-free, with the temperature fixed at z_2 and its vertical derivative (and hence F_T) imposed at z_4. We impose periodic conditions for all the variables on the bounding surfaces at $x = 0$ and $x = A$, where A is the aspect ratio of the horizontal to the vertical dimension of the unstable layer.

Interpretation of the solutions is aided by equations describing the horizontally averaged work terms and fluxes of energy. The evolution of the kinetic energy E can be obtained by forming the dot product of the velocity vector with the momentum equation (2.4), followed by a horizontal average, to yield

$$\frac{\partial E}{\partial t} + \frac{\partial}{\partial z}(F_K + F_P + F_V) + E_B + E_P + E_V = 0\,, \tag{2.10}$$

involving in turn the kinetic, pressure, and viscous fluxes,

$$F_K = -\frac{1}{2}\frac{\gamma + 1}{\gamma}Q\overline{\rho w u_i u_i}, \quad F_P = \frac{\gamma + 1}{\gamma}Q\overline{wP'},$$

$$F_V = \frac{\gamma + 1}{\gamma}Q\overline{u_i\tau_{i2}}\,, \tag{2.11}$$

and the buoyancy, pressure, and viscous rates of working,

$$E_B = (m_2 + 1)\frac{\gamma + 1}{\gamma}Q\overline{w\rho'}\,, \quad E_P = \frac{\gamma + 1}{\gamma}Q\overline{P'\frac{\partial u_l}{\partial x_l}},$$

$$E_V = -\frac{\gamma + 1}{\gamma}Q\overline{\frac{\partial u_i}{\partial x_j}\tau_{ij}}\,. \tag{2.12}$$

The overbar denotes horizontally averaged quantities, the prime denotes the fluctuations about these averages, and angle brackets will be used to denote time-averaged quantities. The

total energy flux is the sum of the kinetic flux F_K, the viscous flux F_V, the convective flux F_C, and the radiative flux F_R, with the latter two expressed as

$$F_C = -Q\overline{\rho w T'}, \quad F_R = \frac{K(z)}{K_2}\frac{\partial \bar{T}}{\partial z}. \tag{2.13}$$

2.3. *Transport of a Passive Scalar*

We will wish to assess the ability of the penetrative convection to mix material in the stable region. We will do so by introducing a passive tracer element into the flows at some time when the convection has arrived at a mature state in which it is statistically steady. We then introduce into the flow a horizontally uniform distribution of this passive element with a specific concentration (by unit mass) of C, taking $C = 0$ outside of the unstable layer and $C = 1$ within it. We study the temporal evolution of C by solving the evolution equation

$$\frac{\partial(\rho C)}{\partial t} + \frac{\partial}{\partial x_j}(\rho u_j C) + \frac{\zeta}{Q}\frac{\partial^2 C}{\partial x_j^2} = 0, \tag{2.14}$$

together with our equations (2.3)–(2.5). A modest diffusion operator is included solely to stabilize the numerical scheme: we typically take the constant diffusion coefficient to be $\zeta = 0.1$, namely 1/10 of the thermal diffusion.

2.4. *Numerical Methods*

We have obtained our fully nonlinear solutions by numerical finite-difference techniques using a two-step Lax-Wendroff scheme, modified to include diffusion of vorticity and heat (see HTM and Graham 1975 for details). We have carried out the majority of the computations with 161 mesh points in the vertical and 121 points in the horizontal. Given our uniform vertical grid and its typical spacings, we are restricted in the degree of nonlinearity and stratification that we can attain by the need to maintain adequate spatial resolution of the decreasing scale height at the top of the layer and of the associated boundary layers. Thus the Rayleigh numbers are typically $\hat{R} = 10^5$. The small vertical scale heights near the top of the computational domain mean that χ_2 should be no larger than about 21 in these simulations. We have found that the solutions are generally time dependent.

Once the convective motions set in, the stable and unstable layers approach overall thermal equilibrium only very slowly. While the thermal stratification in the region of strong convective motions has an initial adjustment which is relatively quick (only a few overturning times), the final thermal equilibration proceeds on a much longer timescale, which is comparable to the Kelvin-Helmholtz time. Further, the lower stable layers have a far greater heat capacity than the unstable layer and consequently possess thermal adjustment times that are several hundred times longer than that of the unstable layer. Since the response times of the two layers are thus quite disparate, we have accelerated the overall thermal relaxation by readjusting the mean temperature gradient occasionally, and thus the radiative flux, within the quiescent region to be that specified at the lower boundary. Such incremental but small adjustments were imposed a few times early within a given simulation, leading to time-averaged total fluxes, $\langle F_T \rangle$, which varied at most by a few percent over the full range of depths. The times indicated here in displaying the solutions correspond to the elapsed time over which we have explicitly computed the solutions from the last discrete adjustments made to the thermal stratification early in the evolution.

3. RESULTS

The structure of convection both within the unstable zone and in the stably stratified layer beneath it is influenced both by effects of compressibility and by the relative stabilities S of the unstable and stable regions. Here we will focus on the influence of the latter, fixing the initial density contrast across the unstable layer (ratio of density at the bottom to that at the top) at $\chi_2 = 6$. This value of χ_2 is large enough to exhibit the effects of compressibility (see Hurlburt et al. 1984) without taxing our computational budget. A few simulations with χ_2 ranging up to 21 were carried out which show behaviors much like the ones to be displayed here (see HTM for solutions with smaller χ_2). All simulations discussed here possess the same Rayleigh number, $\hat{R} = 10^5$, and polytropic index, $m_2 = 1$. We will investigate how the structure of the convection is modified as we change the aspect ratio A from 4 to 8 and the relative stability S from 1 to 15 (and, correspondingly, m_3 from 2 to 9). We have found that the lower stable layer must have at least twice the depth of the unstable layer for there to be sufficient room for the penetrating flows over this range of parameters.

3.1. *Linear Stability Analysis*

We have performed linear stability analysis of such two-layer systems to determine the critical Rayleigh numbers $\hat{R}_c$ for the onset of direct (nonoscillatory) convection as a function of both S and horizontal wavenumber $a = 2\pi/A$. Figure 1 maps out these linear stability boundaries for three values of S. For large a (narrow cells in the horizontal), the convection rolls have negligible penetration into the stable layer, and thus the three neutral stability curves nearly coincide. For small wavenumbers (cells of large horizontal extent) the effects of penetration on the convection rolls cause the three curves to diverge, and for $A = 4$ ($a = \pi/2$) the critical Rayleigh number $\hat{R}_c$ for $S = 15$ is roughly 4 times that for $S = 1$.

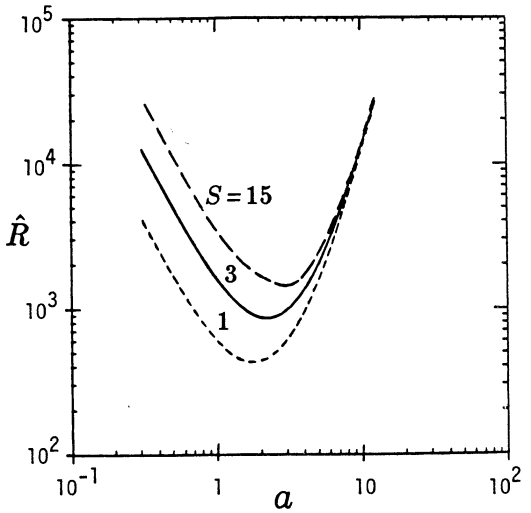

FIG. 1.—Neutral stability curves for the onset of convection, showing the Rayleigh number $\hat{R}$ vs. horizontal wavenumber a for the onset of convection within an unstable layer of density contrast $\chi_2 = 6$ and polytropic index $m_2 = 1$, bounded below by a stable layer whose polytropic index is $m_3 = 2$, 3, and 9 (corresponding to $S = 1$, 3, and 15).

3.2. *General Features of Penetrative Convection at S = 3*

We shall begin our nonlinear survey by considering the behavior of the penetrative convection with $S = 3$, and subsequently turn to cases with other relative stabilities S. Figure 2 displays a typical sequence of events at three successive instants in time in an evolved solution. The velocity fields are shown in the left panels, using randomly positioned arrows which possess lengths proportional to the local velocities and which parallel the local instantaneous streamlines. The associated relative density fluctuations $\Lambda = \rho'/\bar{\rho}$ are displayed as surface perspective plots in the right panels. The motions here are quite complex and show rapid variations with time. The penetrative convection is characterized by narrow and fast plumes which descend across the unstable layer and well into the stable one. These represent coherent flows that span multiple scale heights in the vertical, but the plumes tend to tilt and turn as they descend, and this may confuse the assessment of vertical correlation lengths for such convection. The gravity waves are revealed in Figure 2 both by the oscillations of the density surfaces and by reversing circulations deep within the stable layer. Indeed, the overall time dependence here is much like that in HTM: analysis of the wave field in the middle of the

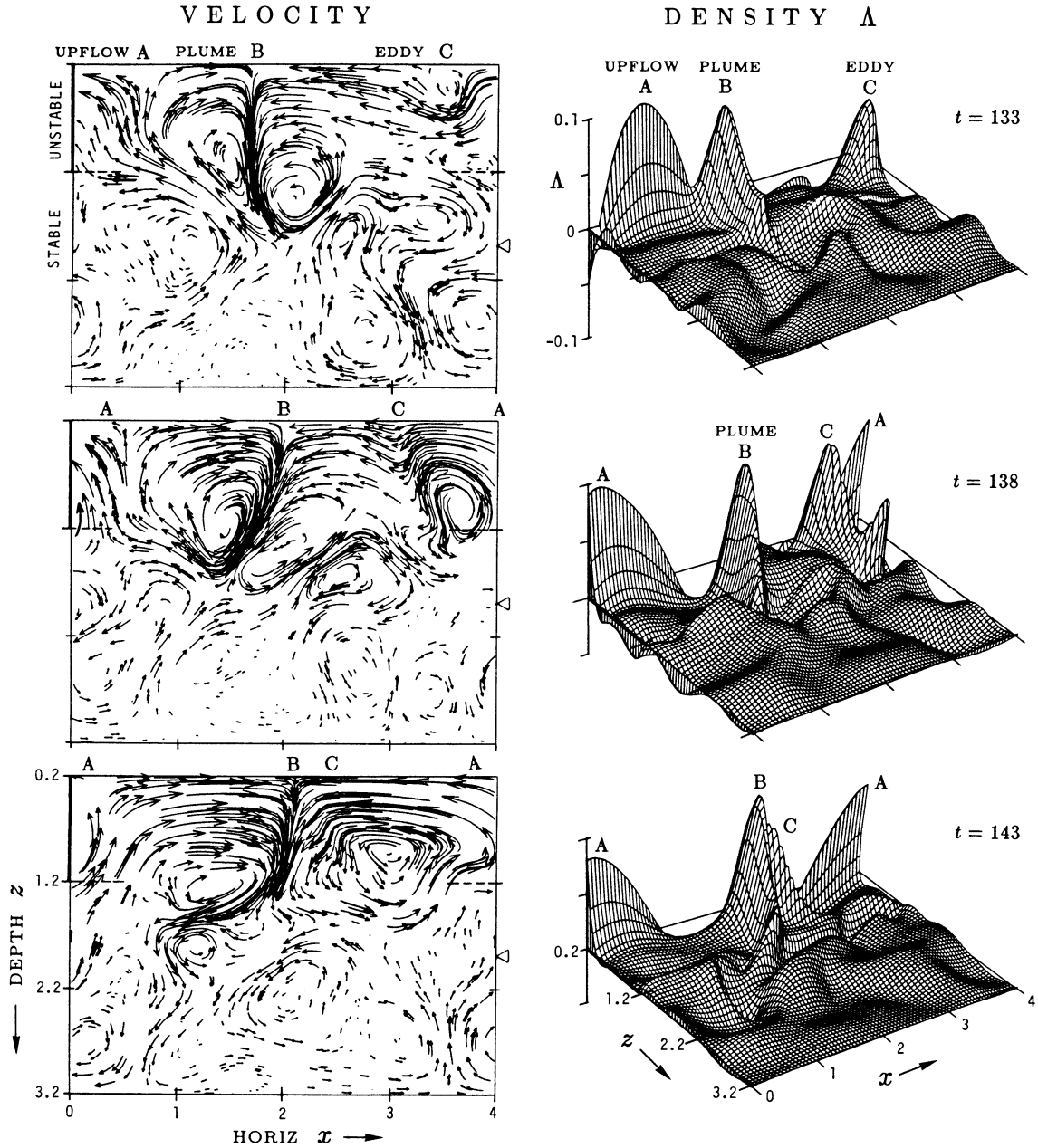

FIG. 2.—Time-dependent nonlinear penetrative convection in an unstable layer bounded below by a region of stable stratification, with a relative stability parameter $S = 3$. Left panels illustrate the velocity streaklines at three instants in time, and right panels the associated relative density fluctuations as perspective surface plots. The prominent downward plumes excite internal gravity waves within the lower stable region, as evidenced by oscillations of the density surfaces. The convection remains vigorously time dependent as the waves feed back upon the plumes, serving to swing them back and forth and to modulate their entrainment. The time interval spanned by these three samples corresponds approximately to one overturning time of the convection. The extent of penetration (as measured by Δ) is indicated by the triangular pointer.

lower layer 3 reveals that most of the power resides in frequency ν between $0.03 < \nu < 0.10$. This indicates that internal gravity waves are clearly present, for such waves are constrained to have frequencies less than the typical Brunt-Vaisala buoyancy frequency $N_3 \simeq 0.10$ at that depth. Further, linear wave analysis reveals that several peaks in the spectrum correspond to the eigenfrequencies for internal gravity modes of the stable layer. In contrast, the time dependence in the unstable layer 2 is representative of slowly modulated convection.

A downward-directed plume (labeled B) persists for a lengthy interval, continually swaying to and fro. The plume B is surrounded by much gentler and broader upflows A. The asymmetries in the vertical flows come about because the pressure fluctuations work in phase with temperature at the sites of downflow to accentuate the density fluctuations and thereby enhance the buoyancy driving, while they work against temperature at the sites of upflow to reduce the driving (see also Massaguer & Zahn 1980; Hurlburt, Toomre, & Massaguer 1984). Such plumes penetrate well into the stable layer and generate a broad spectrum of internal gravity waves there, and these waves in turn deflect the plumes laterally back and forth in time. Overall, the velocity fields here are similar to those found in HTM, even though the initial density contrast has increased by a factor of 3 to $\chi_2 = 6$, and the density contrast of the stable layer has nearly doubled to $\chi_3 = 6.2$. The density and pressure contrasts across the computational domain are $\chi = 37$ and $\chi_p = 407$, respectively, or 6 pressure scale heights. One significant difference with results from the previous simulations in HTM at lower density contrasts is that here the Mach number attained by the flows is considerably greater, for the plumes can reach vertical Mach numbers of about 0.6, and the incoming horizontal flows which feed such plumes occasionally approach total Mach numbers of order unity. We expect such flows to become supersonic for even larger density contrasts and Rayleigh numbers (e.g., Cattaneo et al. 1990; Malagoli et al. 1990).

It is interesting that individual plumes, once established, are able to survive for many convective overturning times. The persistence of some of the plumes is aided by the sweeping away of potential competitors, much as that of eddy C in Figure 2. This eddy begins as a disturbance in the upper thermal boundary layer at $t = 133$ and grows into a plume by $t = 138$. However, before it can fully establish itself, it is swept into the established plume A by the rapid horizontal motions, and thus has nearly vanished by $t = 143$. Hence the evolution of the horizontal scale of the convection is influenced both by the growth rate of small eddies that might grow into full-blown cellular flows (few make it) and the time taken to horizontally advect such competing eddies into the established plume.

The surface plots of the relative density fluctuations Λ in the right-hand panels of Figure 2 reveal two aspects of the dynamics within the unstable layer. First, large density fluctuations are associated with the plume B and eddy C and also with the upflow A near the upper boundary. The latter is a signature of buoyancy braking in the upflows, and this comes about because pressure fluctuations associated with deflecting the vertical flows laterally as they approach the upper stagnation point serves to overwhelm the effect of temperature fluctuations on density there. Second, the eddy C at $t = 133$ possesses a density fluctuation Λ somewhat like that of plume A, although shallower in extent. By $t = 138$ their density perturbations are comparable throughout the unstable layer, but by $t = 143$ these two density features have nearly merged. Thus the plume B has survived, though with modulation in its strength. During the course of such adjustments, the upflow A is in turn modified, accentuated by changes in the recirculation as the plume B swings laterally.

3.3. *Time-averaged Convective Properties*

Although such penetrative convection displays vigorous time dependence involving swaying plumes and gravity waves, it also possesses time-averaged properties which are statistically stable. In Figure 3 we present time-averaged mean fields, energy fluxes and rates of working, indicating those by angle brackets. The radiative flux $\langle F_R \rangle$ in Figure 3*b* approaches unity both at the bottom (at z_4, where it is imposed as a boundary condition) and at the top (z_2). Indeed, we find that the sum of $\langle F_K \rangle$, $\langle F_C \rangle$ and $\langle F_R \rangle$ is almost constant across the computational domain, with the small variation compensated by the small viscous flux (not shown). Similarly, time averages of the total work done on the system should be in balance, with the net contributions of the buoyancy, pressure, and viscous rates of working vanishing. An explicit integration of those terms in Figure 3*c* shows this to be the case.

In analyzing the dynamics of such penetrative convection in Figure 3, it becomes clear that there are three distinctive regions of behavior with depth. Namely, an unstable layer extending from $z = 0.2$ to $z = 1.2$, then a region of active penetration by the plumes from $z = 1.2$ to about $z = 1.88$ (denoted by the triangular pointer), and finally a deeper region below that depth which is dominated by the field of gravity waves. The superadiabatic and subadiabatic stratification that is achieved is evident in Figure 3*a*, which shows profiles with depth of time averages of both the mean density $\langle \bar{\rho} \rangle$ and of the vertical gradient of mean entropy $\langle \partial \bar{s}/\partial z \rangle$, where the entropy $s = \ln(T^{m_a}/\rho)$. The time-averaged radiative flux $\langle F_R \rangle$ in Figure 3*b* is near its adiabatic limit of 0.8 throughout much of the unstable layer, as is expected of efficient convection. The remaining energy flux in this layer is carried upward by the convective or enthalpy flux $\langle F_C \rangle$, which is counteracted in part by the energy carried downward by the kinetic flux $\langle F_K \rangle$. The latter arises from the asymmetry of the vertical flows, with the fast downflows serving to control the sense of the kinetic flux. These two fluxes reach their extrema at the base of the unstable layer, attaining there $\langle F_C \rangle = 0.39$ and $\langle F_K \rangle = -0.20$, which agree well with results from the single-layer simulations of Hurlburt et al. (1984). Hence, much of the transport within the unstable layer is unaffected by the presence of the stable layer beneath it.

We see in Figure 3*c* that the buoyancy work $\langle E_B \rangle$ in the unstable layer is the primary source of kinetic energy, attaining there a peak value of 0.38, whereas viscous dissipation $\langle E_V \rangle$ is the primary sink of energy, possessing values of about -0.16 near the base of that layer. The pressure work $\langle E_P \rangle$ is modest, with a peak of 0.05, but it is positive throughout the unstable layer and hence assists buoyancy in driving the flows. Clearly the three rates of working do not sum to zero in the unstable layer. Hence, the kinetic and pressure fluxes must serve to transport mechanical energy into the stable domain below; that flux $\langle F_K \rangle$ directed downward into the stable region has a crucial role in the extent of penetration achieved by the convection.

Turning to the region of active penetration, we see that $\langle F_R \rangle$ rises rapidly to a peak value of 1.38, which, though considerably greater than that in the static state, is still somewhat below the adiabatic limit of 1.60 for such an $m_3 = 3$ polytrope.

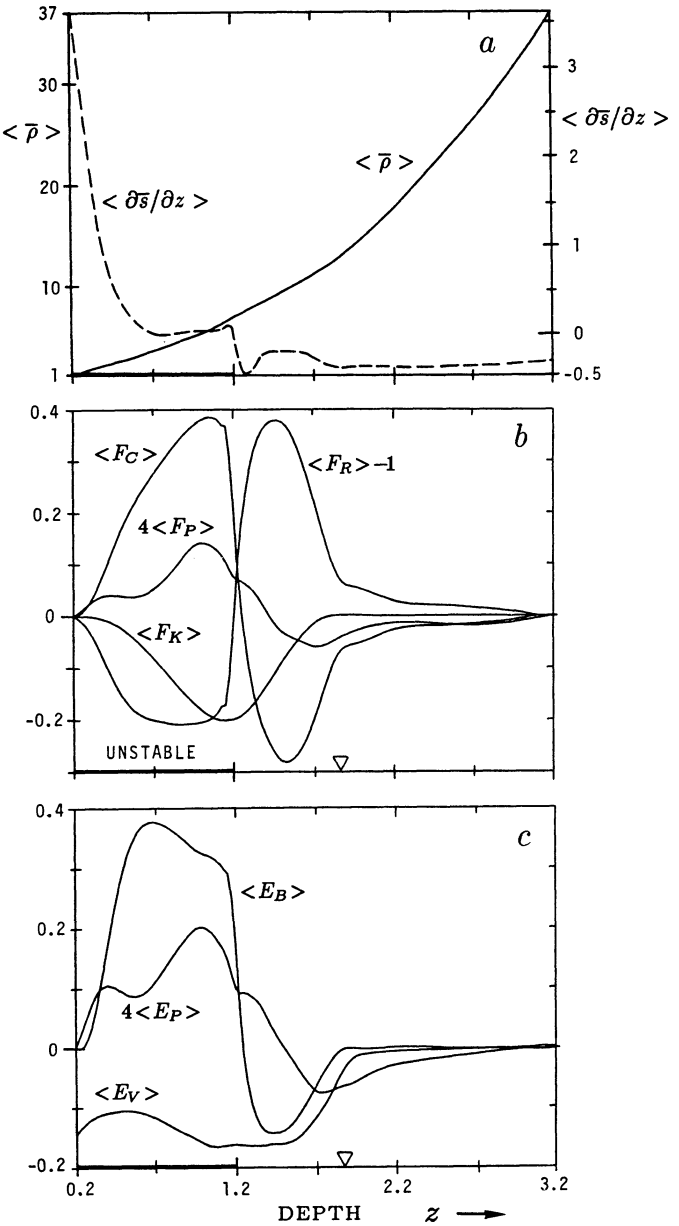

FIG. 3.—Time-averaged convective properties with depth z for the $S = 3$ simulation depicted in Fig. 2. Displayed in (*a*) are the time-averaged mean density $\langle\bar{\rho}\rangle$ and the vertical gradient of mean entropy $\langle\partial\bar{s}/\partial z\rangle$; in (*b*) are the time-averaged radiative flux $\langle F_R\rangle$, convective flux $\langle F_C\rangle$, kinetic flux $\langle F_K\rangle$, and pressure flux $\langle F_P\rangle$; and in (*c*) the associated time-averaged buoyancy $\langle E_B\rangle$, compression $\langle E_P\rangle$, and viscous $\langle E_V\rangle$ rates of working. The total flux F_T has been subtracted from $\langle F_R\rangle$, and $\langle F_P\rangle$ and $\langle E_P\rangle$ have been multiplied by a factor of 4 to make their variations more evident. The time averages are formed over the interval $t = 115$ to $t = 190$, which is also the interval shown in Figs. 7 and 8.

This increase in the upward-directed radiative energy flux is counteracted both by the downward-directed kinetic flux $\langle F_K\rangle$ and by the convective flux $\langle F_C\rangle$ which has changed its sense. It is interesting that $\langle F_C\rangle$ changes its sign at a short distance into the stable region rather than at the interface itself. This comes about from advective effects within the descending flows in the plume which delay the change of sign of temperature fluctuations beyond that interface. The viscous dissipation $\langle E_V\rangle$ attains its extremum near the interface between the layers and is almost constant over much of the region of penetration. The buoyancy work $\langle E_B\rangle$ changes sign close to the interface, thus leading to a pronounced decrease of kinetic energy with depth as the flows are being decelerated. Indeed, by a depth of $z = 1.88$ the plumes have been stopped or turned aside, if we are to judge from $\langle F_K\rangle$, and below that depth there is only a small convective flux $\langle F_C\rangle$ and pressure flux $\langle F_P\rangle$ associated with the internal gravity wave field. One estimate of the penetration depth Δ may be the distance below the interface z_2 where the first zero of the kinetic flux $\langle F_K\rangle$ is achieved and that yields a value of $\Delta = 0.68$ for this case. Such a penetration depth is indicated on all the figures by a pointer triangle.

3.4. *Effects of Aspect Ratio A*

The simulation described above effectively contains one evolving convection cell within its computational domain, and hence may not be representative of dynamics in an infinite horizontal domain. To assure ourselves that our choice of aspect ratio is not influencing our conclusions unduly, we have also considered differing values of A. A complete exploration is beyond the scope of this study. However, we present in Figure 4 one simulation with $A = 8$ which was begun from the same initial conditions as that of Figure 3 and evolved until the flows attained a statistical steady state.

The increase in aspect ratio by doubling the lateral extent of the domain has clearly led to more complex flows. The velocity fields, again displayed through randomly positioned streaklines in Figure 4, reveal the presence of at least one persistent plume at B and one persistent site of upflow D. Hence, we can argue that the overall flows once again have an aspect ratio comparable to that of the computational domain. However, the two secondary eddies at A and C are significant competitors. Both are relatively long-lived structures, though both are seen to be gradually advected away from the upflow site D into the established plume B during this time sequence. At some other intervals there were two plumes in residence, but typically one was more persistent. Clearly the apparent horizontal scale of such two-dimensional convection is dominated by the positioning of the plumes, and with wider domains they can be distributed more randomly; this affects the manner in which secondary eddies survive, and may even end up prevailing.

Although the change in aspect ratio modifies the scale of flows within the unstable layer, it has a much weaker influence on motions within the stable layer. As the competing plumes and eddies merge there are occasional events of apparently deep penetration, as at $t = 163$, but these have little impact in the long run. The spectrum of the gravity wave field in the stable layer is still dominated by waves with $a = 1.57$ (such as fit into the $A = 4$ domain), and the depth of penetration $\Delta = 0.62$ is quite close to the value found above for $A = 4$. Thus we conclude that the primary mechanisms of penetration in such nonlinear flows are reasonably captured by simulations with $A = 4$.

3.5. *Effects of Relative Stability S*

We now turn to the primary goal of this paper, which is to assess how changing the relative stability S of the lower layer influences the extent of penetration into that layer and may modify the vigor of convection in layer 2. We shall consider five simulations with S ranging from 1 to 15. We recall that we are keeping $\hat{R}$ fixed, and since $\hat{R}_c$ increases somewhat with S, there may be a small effect because the ratio $\hat{R}/\hat{R}_c$ changes. The

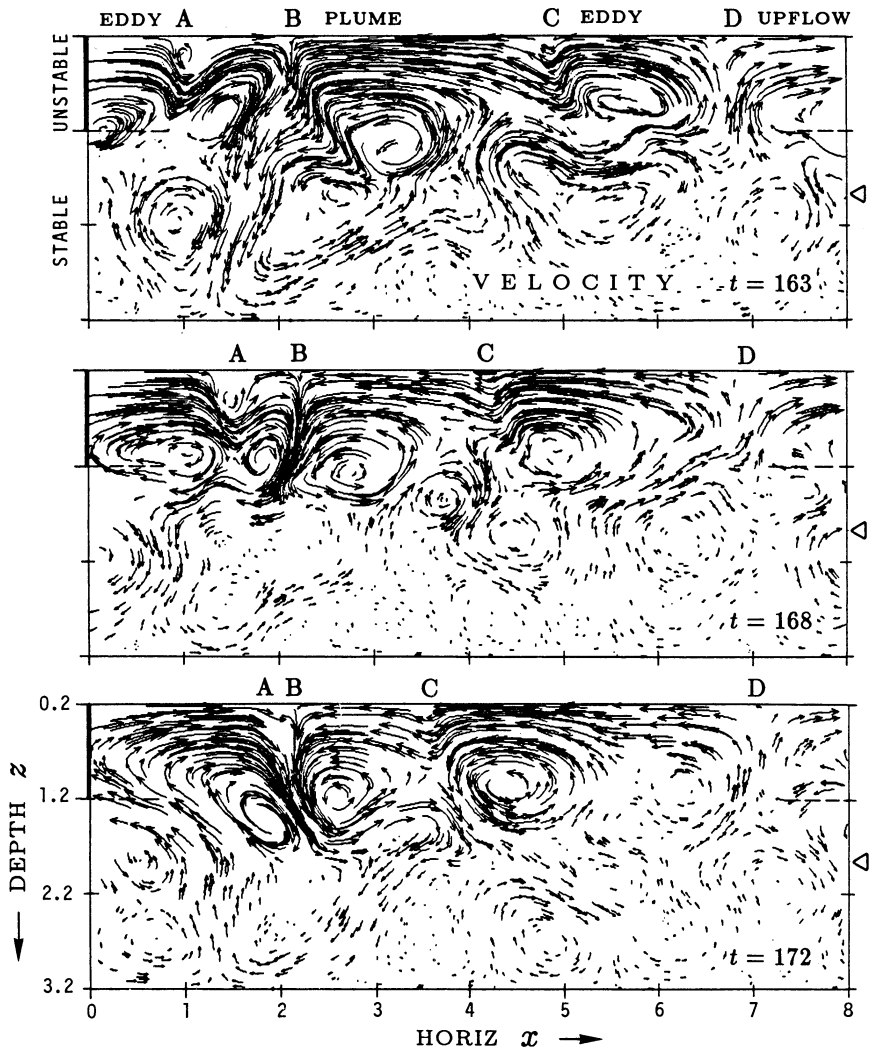

FIG. 4.—Velocity fields for time-dependent penetrative convection for $S = 3$ with a wider computational domain of $A = 8$, with all other parameters identical to those in Fig. 2. The larger aspect ratio admits larger scale flows in the horizontal, and they are more complex, but such convection has penetrative properties similar to the $A = 4$ solutions in Fig. 2.

characteristic wave field induced in the lower layer will be altered, noting that the buoyancy frequency at the top of the stable layer, $N = (4S/[S + 5])^{1/2}$, increases by about a factor of 2 as S increases from 1 to 15.

3.5.1. *Changes in the Flow Structure*

Figure 5 shows the velocity field at two instants in time for $S = 15$ ($m_3 = 9$) in which the lower layer possesses the most stable stratification. Once again the flows are dominated by strong, narrow, downward plumes and broad regions of upflow. The strength of the plume is comparable to that displayed in Figure 2 and, hence, the increased stability of the stable layer appears to have little influence on the development of such plumes in the unstable layer. It does, however, have a significant influence on the ability of the plumes to penetrate into the stable layer. Here we find a reduced penetration depth with $\Delta = 0.31$. Further, the wave field below appears much weaker. This is partly due to the rapid increase in density with depth in this solution, but we will see below that the mechanical energy of the wave is also very small there. Hence the coupling between the convection and the gravity wave field has decreased as S has increased.

One intriguing feature of convection in such stiff systems can be seen in the second panel ($t = 128$) of Figure 5. The plume there is turned sharply as it enters the stable layer and, indeed, is deflected back into the unstable layer as an upward-directed plume. The plume conserves most of its mechanical energy and returns it into the unstable layer. Thus it is not surprising that little energy is transferred into the wave field below.

At the other extreme, we show in Figure 6 the velocity field for $S = 1$ ($m_3 = 2$) in which the stable layer is nearly adiabatically stratified. The plumes extend far into the stable layer under these conditions. In order to accommodate this increased depth of penetration, we have increased the computational domain to $z_4 = 4.2$. The character of the flows has changed significantly from the previous cases. There is much more interaction and competition between the plumes generated within the unstable layer. We can see two plumes (A, C) and two sites of upflow (B, D) at $t = 154$. By $t = 164$ the site of upflow B and the plume A have collided as plume A is being

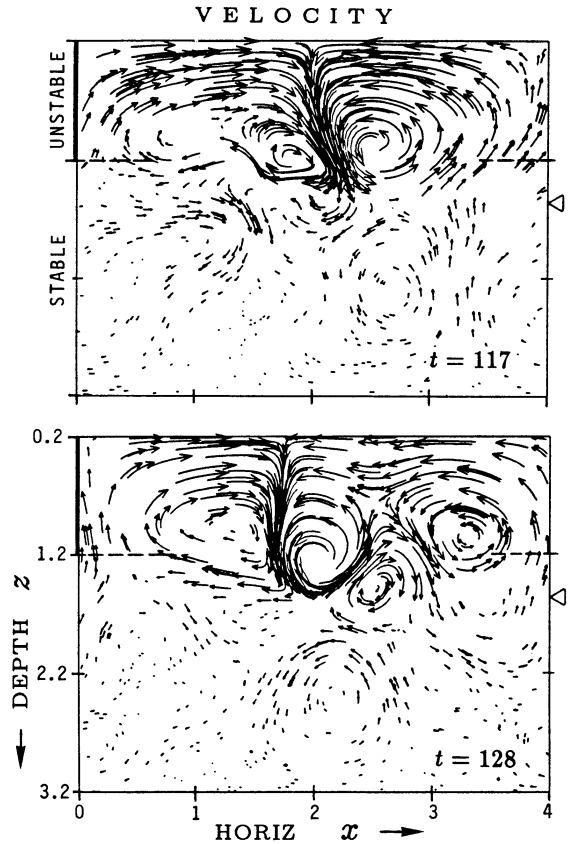

FIG. 5.—Velocity field for $S = 15$ at two instants in time t for convection penetrating into a very stable layer where $m_3 = 9$. With such a stratification, the extent of penetration is sharply diminished, and the gravity wave field is weaker. Although $\hat{R} = 10^5$, the critical $\hat{R}_c$ has increased with m_3, and here $\hat{R} \simeq 50\hat{R}_c$.

slowly advected toward plume C. This advection is slow compared to the dynamics of the flow, and it is not obvious which plume will win; typically, for $S = 1$ several plumes are present at any given time.

The concept of cellular convection is considerably taxed by these flows for $S = 1$. It may be more useful to consider the flow as a set of thermals or plumes (some short-lived, others more persistent) which transit the unstable layer and plunge deep into the stable one. These thermals are closely coupled to the gravity wave field below, and it is quite difficult to make a clear distinction between a region dominated by penetrative convection and a region dominated by waves. Using the previous definition of penetration depth, we find here that $\Delta = 1.85$.

3.5.2. *Changes in the Dynamics*

The differing dynamical behavior in the previous two simulations can be interpreted by turning to the variations with depth and time of the kinetic energy density E and the kinetic energy flux F_K. Although these two quantities are closely related, the kinetic energy density $E \propto \overline{u^2 + w^2}$ is dominated by the horizontal component of velocity u, which is significant over much broader regions than the vertical component. In contrast, the kinetic flux $F_K \propto \overline{w(u^2 + w^2)}$ is dominated by the contributions of the vertical velocity w due to the weak spatial correlation between it and the horizontal component u. That

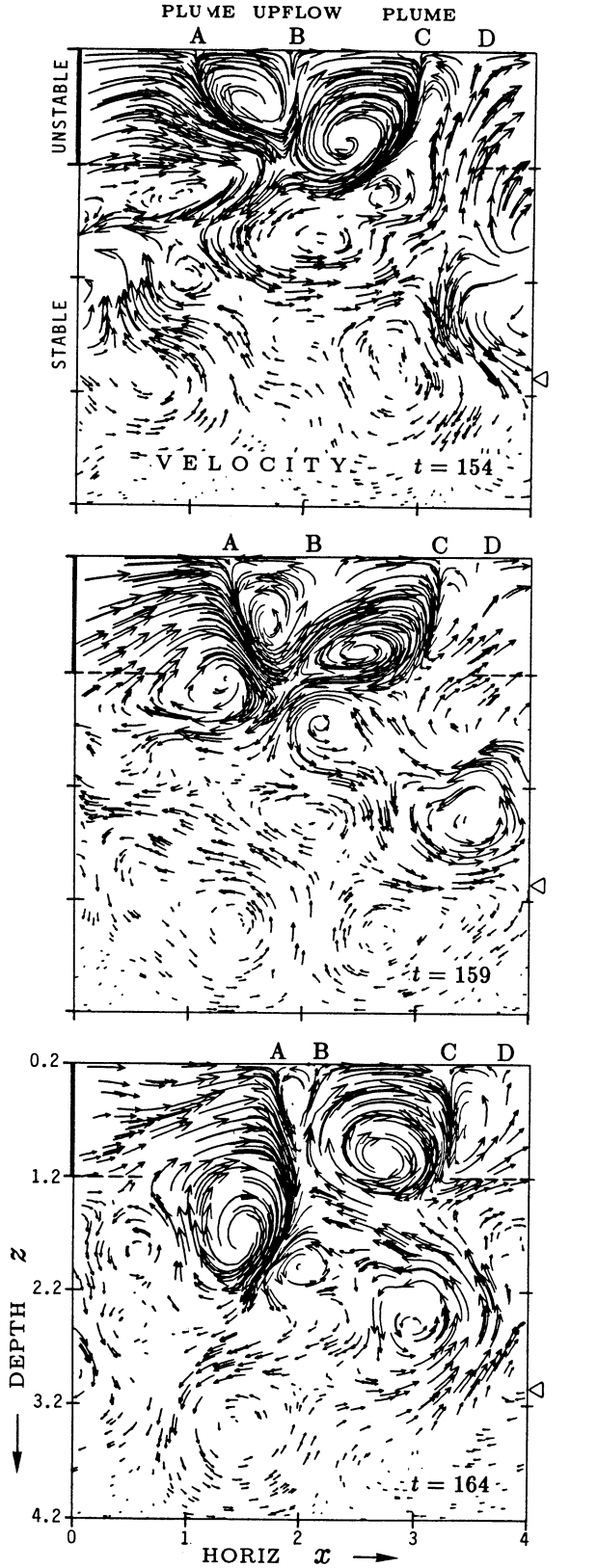

FIG. 6.—Velocity field for $S = 1$ at three instants in time t for convection penetrating into a mildly stable layer where $m_3 = 2$. The computational domain is here deeper to be able to accommodate the extensive penetration and strong gravity wave field in the region of weak stratification. Here $\hat{R} \simeq 200\hat{R}_c$.

flux will be directed downward, reflecting the asymmetry of the vertical flows which involve fast downflowing plumes.

We present in Figure 7 the kinetic energy density E, and in Figure 8 the kinetic energy flux F_K, as functions of time t and depth z for three values of S. Each curve in depth is offset vertically by a distance proportional to the time. Hence structures propagating downward in the simulations appear in these figures as features traveling upward and to the right. When the relative stability is large ($S = 15$), we see in Figure 7*c* that the kinetic energy distribution E varies only moderately with time; its peak is located at a depth $z \approx 1.4$. The sharp peak is due to the strong horizontal flows generated there as the plume is turned abruptly by the stiff stratification. Virtually all of the energy resides in the unstable layer and in the relatively shallow region of penetration just below it. The energy density below $z = 1.7$ is negligible, for the wave field is very weak there. The kinetic flux F_K for $S = 15$, displayed in Figure 8*c*, is somewhat more dynamic; pulses of moderate amplitude repeatedly transit the unstable layer. Since E is largely a measure of the horizontal velocity and F_K that of the vertical velocity, taken together they suggest that the horizontal velocities are reasonably steady for $S = 15$ and that the flows are only slightly modulated by pulsations in the vertical plumes. There is little interaction between this convection and the weak gravity wave field beneath it.

The picture changes significantly as we turn to the $S = 1$ solutions in Figures 7*a* and 8*a*. (Whereas the lower computational boundary for these solutions is located at $z_4 = 4.2$, we only display the region above $z = 3.2$ for comparison with the other simulations.) Here we find large variations of the kinetic energy E with both time and depth, and these profiles for E extend far below the unstable layer. Indeed, both the peak value of E and the bulk of the total kinetic energy reside well

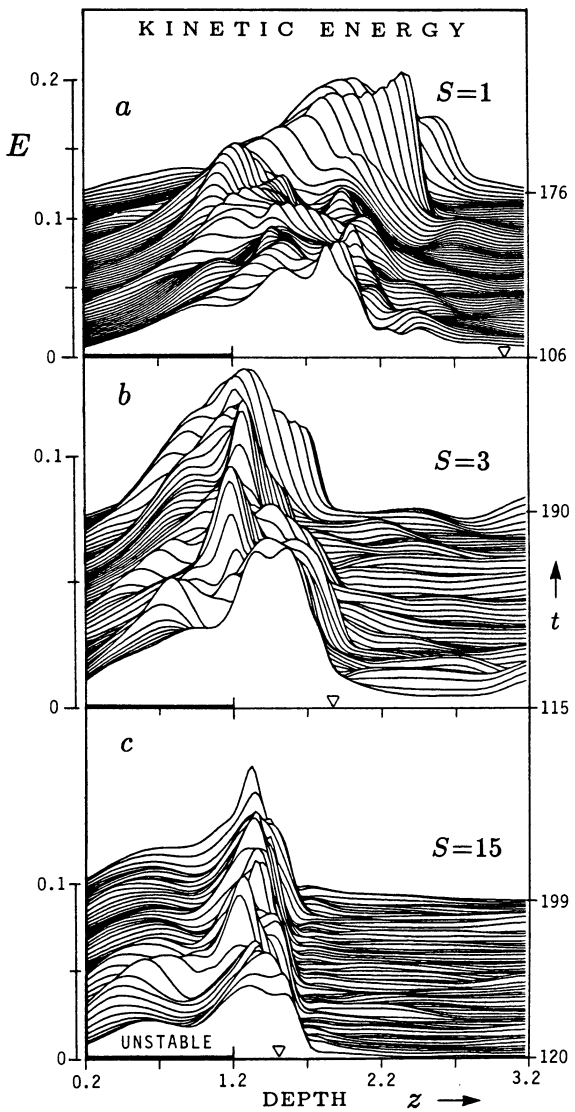

FIG. 7.—Kinetic energy density E as a function of time t and depth z for the simulations in Figs. 2, 5, and 6. For clarity, each successive curve in time is offset upward from its predecessor by a fixed increment. (*a*) For $S = 1$, the convective flows penetrate very deeply (with that depth of penetration delineated by the triangular pointer), with E exhibiting major pulses far into the stable layer. (*b*) For $S = 3$, E varies prominently in time, with noticeable fluctuations in the deeper regions due to the wave field. (*c*) For $S = 15$, the kinetic energy peaks near the interface between the unstable and stable layers and then falls off rapidly with depth.

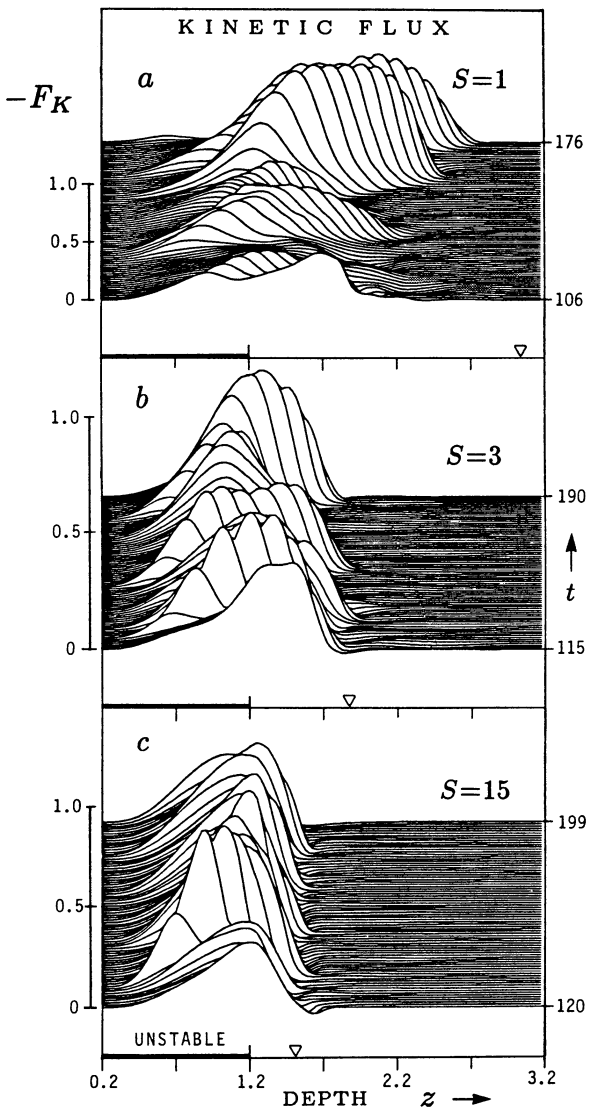

FIG. 8.—Comparison to Fig. 7, showing the kinetic flux F_K as a function of time t and depth z for the $S = 1$, 3, and 15 simulations.

within the stable layer at all times. Descending pulses in E repeatedly cross the unstable layer and travel into the lower layers. Similar behavior is evident in the kinetic flux F_K in Figure 8*a*, with that flux dominated by large pulsations which are carried downward with time. These pulses not only grow in amplitude within the unstable layer, as one might expect, but also for a significant distance into the stable layer: they occasionally coast far into that layer with little dissipation. The kinetic energy density E possesses comparable peaks which descend with these pulses in the kinetic flux F_K. Thus the descending elements in these flows are relatively self-contained. They appear as isolated eddies or thermals which can sustain deep excursions into the stable material.

Detailed inspection indicates that the plumes are able to maintain their coherent structures over their deep transit into the stable layer, depositing their energy finally over a narrow interval in depth. The particular depth achieved for any given pulse is somewhat controlled by the steering of the plume by the wave field, though on average it is determined by buoyancy braking over its transit and appears to be influenced by the fluid that it entrains. These prominent pulses emphasize that such penetrative convection is highly nonlocal, for the plumes are able to deposit energy deep within the stable layer.

These excursions into the stable layer result from the ability of the convection to saturate the restoring force of buoyancy. As noted by Massaguer et al. (1984), the close relationship between the rate of buoyancy working, $E_B \propto \overline{w\rho'}$, and the convective flux, $F_C \propto \overline{wT'}$, places a limit on the magnitude of the restoring force available to decelerate the flows. If the convection establishes an adiabatic stratification in the region of penetration, then the convective flux there is constrained to be $|F_C| \lesssim |F_T - F_A|$, where F_T is the total flux and F_A is the radiative flux carried by the adiabatic gradient. As S becomes smaller, F_A approaches F_T, and thus F_C becomes smaller and so does the rate of buoyancy braking in that penetrative region, noting that $F_A = (1 + S/5)F_T$. Thus the $S = 1$ flows experience moderate braking in layer 3, and the pulses extend deeply into that region.

The intermediate case with a relative stability of $S = 3$ shown in Figures 7*b* and 8*b* has some aspects of the other two solutions. The peak of the energy density E remains relatively stationary at the depth $z \simeq 1.3$, and a reasonable fraction of the total kinetic energy resides within the unstable layer. Yet successive descending pulses in both E and F_K are evident as the plumes strengthen and weaken. At greater depths, E shows oscillations associated with the gravity wave field, yet such waves yield almost no signal in F_K.

3.5.3. *Changes in the Energy Transport*

In studying the range of penetrative convection achieved as S is varied, we went from the $S = 15$ solutions representing modulated cellular convection with modest penetration to the $S = 1$ solutions that exhibit major pulses associated with descending thermals or plumes. We now turn to see what aspects of such a range of behavior survive in the time averages of E and F_K.

The time-averaged kinetic energy density $\langle E \rangle$ and kinetic energy flux $\langle F_K \rangle$ are displayed in Figures 9 and 10 for five values of the relative stability S. The transition between the two forms of penetration is evident. For large S (=7, 15) the kinetic energy density $\langle E \rangle$ in Figure 9 possesses a double-peaked form, with the lesser peak located in the unstable layer and the greater peak at a short distance into the stable layer.

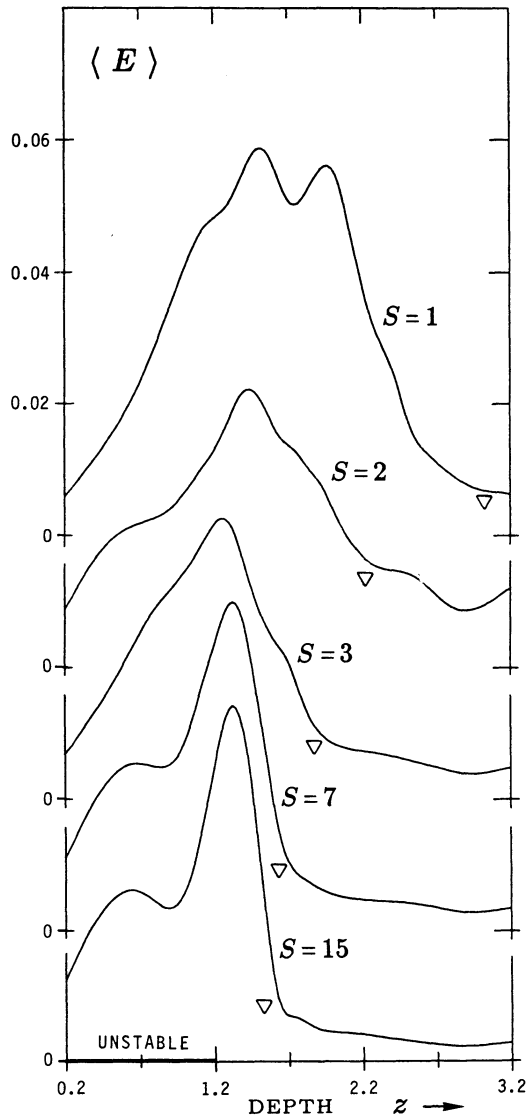

FIG. 9.—Time-averaged kinetic energy density $\langle E \rangle$ as a function of depth z for simulations carried out for five values of the relative stability parameter S, with $S = 1, 2, 3, 7$, and 15.

As in HTM, we find that these double peaks correspond to those of the horizontal velocity. The structure of the horizontal flows here is very reminiscent of that observed in convection within a single layer. The kinetic energy flux $\langle F_K \rangle$ for large S in Figure 10 peaks near the base of the unstable layer and then drops rapidly with depth; the change in the sign of $\langle F_K \rangle$ suggests that an effective small countercell exists just below the main cell, possibly arising from the strongly turned plumes there.

For values of the relative stability S near unity the kinetic energy density $\langle E \rangle$ displays monotonic variation across the unstable layer and attains its maxima well within the stable layer. The increase in $\langle E \rangle$ is roughly proportional to that in mean density in layer 2; hence the flows within the unstable layer involve horizontal velocities which are almost constant with depth. The $\langle F_K \rangle$ curve for small S has its peak located at a short distance into the stable region, and possesses a gradual monotonic decrease with depth, with no effective countercells.

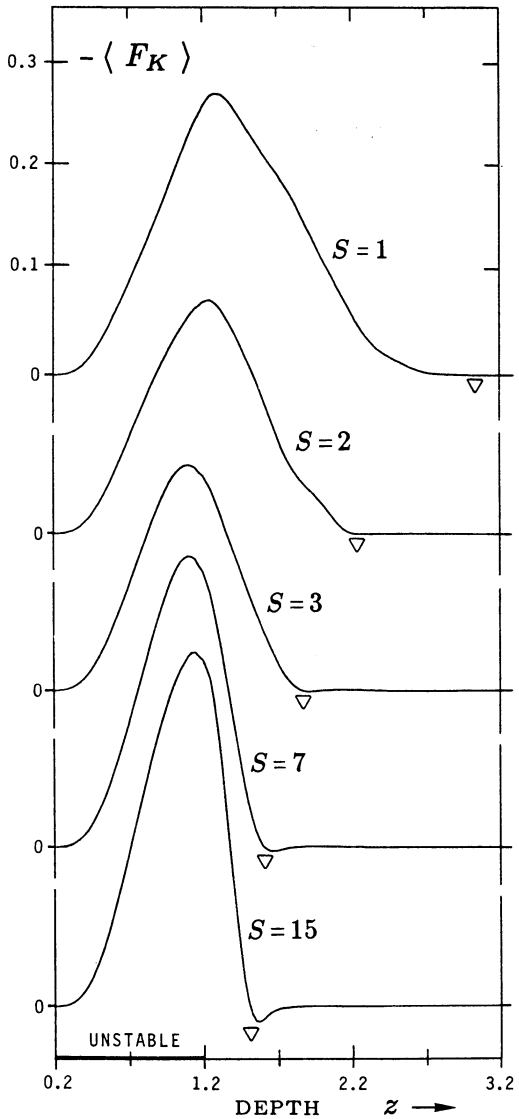

FIG. 10.—Companion to Fig. 9, showing the time-averaged kinetic energy flux $\langle F_K \rangle$ as a function of depth z for five values of S.

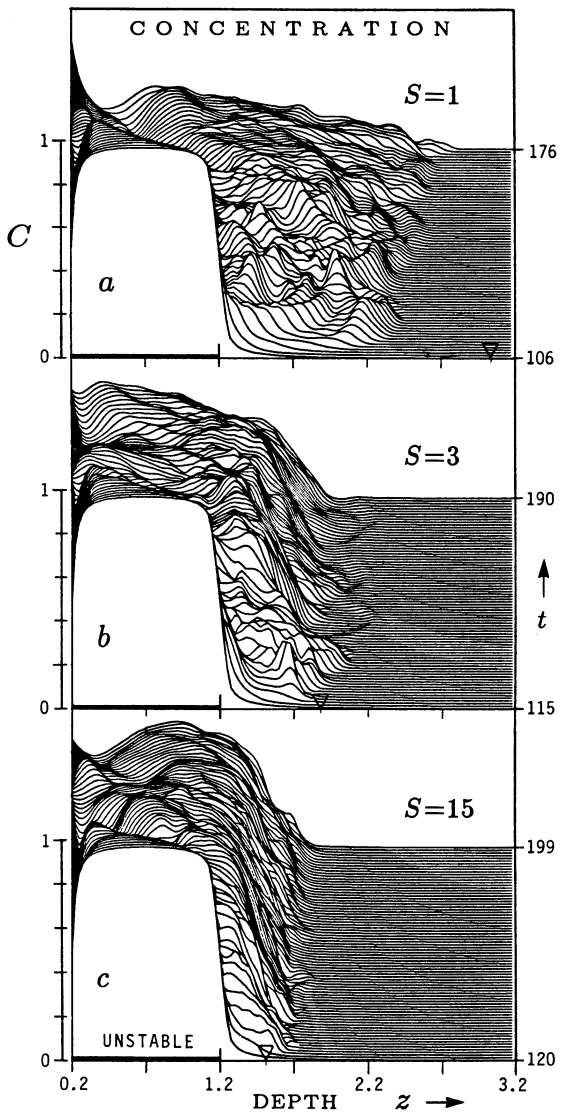

FIG. 11.—Evolution of the concentration C of the passive scalar as a function of time t and depth z in simulations with $S = 1$, 3, and 15.

3.6. *Mixing of a Passive Scalar*

We conducted a series of numerical simulations with a passive scalar field added to the flows (see § 2.3) in order to determine qualitatively how well our measurement of the penetration depth Δ (based on the location of the first zero of $\langle F_K \rangle$ in the stable zone) relates to the depth to which rapid mixing of a species is achieved. In each simulation we added a scalar field with a concentration C per unit mass of zero in the stable layer and unity in the unstable one. This field was introduced into the evolved solutions at time t_0, and then the system including the evolution equation (2.14) was evolved further to time t_f. These times were chosen to correspond to the intervals presented in Figures 7 and 8 for simulations with $S = 1$, 3, and 15. As boundary conditions we imposed a fixed concentration C at the upper and lower boundaries, setting $C = 0$ at z_4 and $C = 0.5$ at z_2; the latter value was chosen to yield little flux of C through the upper boundary in the $S = 3$ simulation.

We present the horizontally averaged specific concentration of the passive scalar C in Figure 11 for these three values of relative stability S. In each case the tracer material C within the unstable layer is rapidly advected down to the penetration depth Δ on a timescale comparable to the plume transit time. After this initial stage, the tracer material within the unstable and penetrative regions begins to slowly equilibrate. For moderate to large S, such as $S = 15$, a sharp concentration gradient develops at the penetration depth and little, if any, material is advected beneath this point. It can, however, diffuse slowly, for we maintain a small diffusive term for numerical stability.

For small relative stability ($S = 1$, 3) the details are again distinctive. In the early stages of mixing, we can clearly see that it is occurring in a series of pulses, corresponding to the isolated plumes injected into the stable layer. These pulses successively carry the tracer downward until the entire region is fairly uniformly mixed. We thus deduce that our measurement of the penetration depth Δ agrees well in all cases with the depth to which material is rapidly mixed in the initial mixing phase. That phase may be followed by a slower one in which other plumes, coupled to the gravity wave field, may carry the material even further downward. However, the assessment of

such transport is rather subtle and is likely to be influenced by whether the wave field is one of standing waves with depth (as imposed by our lower reflecting lower boundary) or rather of propagating waves. Further, the occasional plunging events, even if rare, may contribute substantially to the mixing in the long term, but assessing their role would require simulations extending over far longer timescales than we could undertake.

4. EXTENT OF PENETRATION

The extent of penetration into the stable lower layer can be assessed by various measures, including the penetration depth Δ that we have cited as based on the position of the first zero of the kinetic flux below the interface at z_3. Figure 12 summarizes the variation of Δ with S realized in our sequence of two-dimensional simulations. Clearly the extent of penetration Δ decreases systematically with increasing relative stability S of the stable layer, and there is a suggestion that two different power laws may be involved, with a variation of the form S^{-1} prevalent at the smaller values of S, to be replaced possibly by $S^{-1/4}$ at the larger values of S. This variation encourages us to turn to simpler scaling models for the dynamics to see if they may help to interpret the pattern of behavior for Δ with S revealed in Figure 12.

4.1. *Scaling Laws from a Simple Model*

We can seek to interpret the variation of the extent of penetration Δ with S below a convective layer by considering some simplified models which yield scaling laws for Δ. Though the approximations are rather crude, we can obtain reasonable insight from the models and find good contact with the behavior for Δ shown in Figure 12. A similar approach has been described in Zahn (1991) for the case of a smooth conductivity profile with depth, and it provides excellent agreement with the results of plume calculations (Schmitt et al. 1984). For such profiles the penetration depth scales as $f^{1/2}W_0^{3/2}$, f being a filling factor and W_0 being the velocity of the downward-directed flows, as they enter the adjacent stable layer.

Here we consider instead an envelope in which the conductivity is piecewise constant with depth. One assumption is that

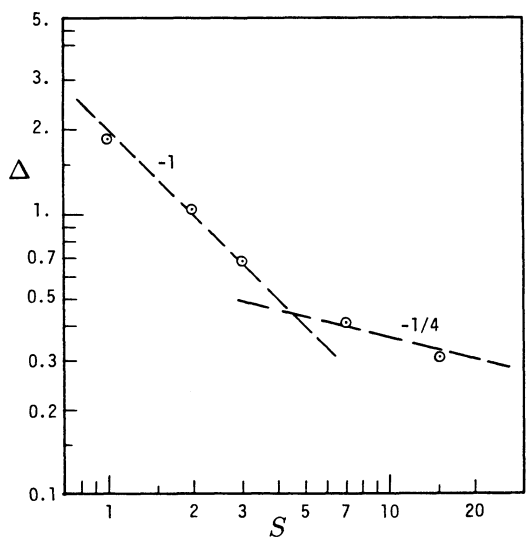

FIG. 12.—Variation of the penetration depth Δ with relative stability parameter S for the five simulations. Possible power laws for two intervals are suggested by the two straight lines.

the convection is efficient enough to establish an adiabatic stratification in the unstable layer. This requires that the Peclet number, $P_e = wl/(K_2/\rho c_p)$, characterizing the motions within that layer is substantially larger than unity (l and w are the typical size and vertical velocity of those motions, $K_2/\rho c_p$ the thermal diffusivity).

There are generally two distinct layers in the region of penetration below the unstable zone. The upper of these two exists only if the local Peclet number P_e based on K_3 is still greater than unity. Let us assume that its stratification is nearly adiabatic, and let us call it the *adiabatic penetration* (P) region. In this region the motions decelerate, due to buoyancy braking, until the Peclet number reaches a value of order unity at depth $z_P = z_3 + l_P$. Below, there is a *thermal adjustment* layer (T) of thickness l_T, in which the temperature fluctuations taper off because of radiative damping. Finally, beyond $z_T = z_P + l_T$, we have the radiative interior, where heat is transported only through radiation.

We shall now use this schematic picture to first estimate the extent l_P of the adiabatic penetration region, using dimensional variables for convenience at this stage. Within that region the radiative flux is the constant

$$F_A = K_3\left(\frac{dT}{dz}\right)_{ad}, \tag{4.1}$$

for we have assumed that the stratification is nearly adiabatic. The convective flux F_C is obtained by subtracting F_A and the kinetic energy flux F_K from the total flux, with

$$F_C(z) = F_T - F_A - F_K(z)\ ; \tag{4.2}$$

that flux is negative, since $F_A > F_T - F_K$.

We shall assume that the fraction f of the area is occupied by downward-directed motions, which transport most of the energy flux, as observed in our simulations. We express that convective (enthalpy) flux to lowest order in terms of the horizontal temperature fluctuations and the vertical velocity of these motions, which we assume to be highly correlated, as

$$F_C = -f\rho c_p W\,\delta T\ . \tag{4.3}$$

The quantities W and δT represent the rms of the vertical velocity and of the temperature fluctuation in the fraction f of the area where these motions occur. In this simple model, we assume that the vertical velocity and the temperature fluctuation have the same horizontal profile, and we ignore the increase of f with depth.

4.2. *Nearly Adiabatic Penetration Region*

To estimate the extent l_P of the nearly adiabatic penetration region, we first follow the downdrafts from $z = z_3$ until they nearly stop at $z_P = z_3 + l_P$. We further assume that their exiting velocity W_0 at z_3 is determined solely by the dynamics in the unstable layer above, and does not depend upon the penetration depth; this is nearly so in the actual simulations discussed above. The deceleration of these flows is described to first order by

$$\frac{c}{2}\frac{dW^2}{dz} = g\frac{\delta\rho}{\rho} = -g\frac{\delta T}{T}, \tag{4.4}$$

with the assumption of pressure equilibrium. The quantity c which appears here is related to the triple moment of the velocity as

$$cf = \frac{\overline{w(u^2 + w^2)}}{(\overline{w^2})^{3/2}},$$

u and w being the horizontal and vertical velocities; here that parameter c is also assumed to be constant in depth.

After elimination of δT with equation (4.3), we obtain the following differential relation

$$\frac{d}{dz}\left(\frac{W}{W_0}\right)^3 = -\frac{3gF_T d}{cfc_p\rho(z)T(z)W_0^3}\left[\frac{m_3 - m_2}{m_a + 1} + \phi_K\left(\frac{W}{W_0}\right)^3\right], \tag{4.5}$$

where ϕ_K is the ratio between the kinetic flux and the total flux at $z = z_3$. In integrating this equation from $W = W_0$ to $W = 0$, while z varies from z_3 to $z_3 + l_P$, we shall take also into account the variation with depth of $\rho T = \rho_2 T_2 (z/z_2)^{2.5}$ in such an adiabatic stratification. The result is

$$\frac{z_3}{1.5}\left[1 - \left(1 + \frac{l_P}{z_3}\right)^{-1.5}\right] = A_P \frac{1}{\phi_K}\frac{m_a - m_2}{m_a + 1} \times \ln\left[1 + \frac{m_a + 1}{m_3 - m_a}\phi_K\right], \tag{4.6}$$

where

$$A_P = \left[\frac{cf}{3}\frac{\rho_3 W_0^3}{F_T}\right]\left(\frac{1 + z_2}{z_2}\right)^{1.5}\frac{(m_a + 1)^2}{m_a - m_2}$$

is independent of m_3 and l_P. In order to determine the value of A_P, we have to calibrate the expression in the brackets, which represents the term $\phi_K/3$, by turning to our actual simulations; indeed, from Figure 10 one can estimate that ϕ_K is approximately 0.25. To lowest order, i.e., for not too small a value of $m_3 - m_a$ (or S), this equation (4.6) reduces to

$$l_P = A_P S^{-1}, \tag{4.7}$$

in terms of our stratification parameter $S = (m_3 - m_a)/(m_a - m_2)$ from equation (2.2). We see that the scaling differs from that obtained when the conductivity varies smoothly at z_3, where $l_P \propto f^{1/2} W_0^{3/2}$ (Zahn 1991).

4.3. *Thermal Adjustment Layer*

We now turn to the thermal adjustment layer (T), which connects the nearly adiabatic region (P) with the radiative interior. To estimate its thickness l_T, we proceed as follows. At $z_P = z_3 + l_P$ the velocity is not strictly zero, as we have pretended above, but the Peclet number characterizing it is of order unity. Hence $cW_P l_T = K_3/\rho_P c_p$ (see Zahn 1991 for the justification of c in this relation); here the subscript P denotes the value of a variable at z_P. In this thermal adjustment layer, the temperature fluctuations decay from their initial value δT_P to zero, and therefore, according to equation (4.4),

$$cW_P^2 \approx c_T g d \frac{\delta T_P}{T_P} l_T, \tag{4.8}$$

where c_T is a constant of order unity (but smaller than 2). Multiplying by W_P, making use of $cW_P l_T = K_3/\rho_P c_p$, and expressing the convective flux by

$$F_C = -F_T \frac{m_3 - m_a}{m_a + 1}, \tag{4.9}$$

since F_K has become negligible at this point, we obtain

$$f\left(\frac{K_3}{\rho_P c_p}\right)^2 = gc^2 c_T d^4 \frac{F_T}{K_3 T_P}\frac{m_3 - m_a}{m_a + 1}(l_T)^4. \tag{4.10}$$

Replacing $g = (m_2 + 1)R_* T_2/z_2 d$ and $(m_3 - m_a)$ in terms of the stratification parameter S, we find that the extent of the thermal layer is

$$l_T = A_T S^{-1/4}, \tag{4.11}$$

with

$$(A_T)^4 = \left[\frac{f}{c^2 c_T}\right] Q^{-2}\left(\frac{z_3 + l_P}{z_2}\right)^{-2}(z_2)^2 \frac{m_a + 1}{(m_2 + 1)(m_a - m_2)}.$$

We have again placed in brackets the term which must be calibrated by the actual calculations, and have introduced the Peclet number constructed with the sound velocity, namely $Q = (R_* T_2)^{1/2} d/(K_2/\rho_2 c_p)$ [from eq. (2.8)]. Note that when S is small, A_T depends somewhat on the adiabatic penetration l_P, through the ratio $(T_P/T_2)(\rho_P/\rho_2)^{-2}$ which is present in equation (4.10).

The total extent of convective penetration is the sum $\Delta = l_P + l_T$. We see that for small S, it is the nearly adiabatic penetration l_P which dominates, whereas for large S the thermal adjustment layer of thickness l_T is the broadest of the two. The crossover from the S^{-1} to the $S^{-1/4}$ law is governed by the parameter Q^2, which is proportional to the Rayleigh number [eq. (2.9)]. For large $\hat{R}$, the thermal adjustment layer shrinks to a thin boundary layer, whereas for small $\hat{R}$, the nearly adiabatic penetration is never achieved and l_T is the only contributor to Δ. Our simulations possess $\hat{R}$ such that both l_P and l_T play a role.

As we increase S, we enhance buoyancy braking, but we also lessen the local Peclet number (by increasing the conductivity K_3), and therefore the penetration depth decreases at a slower pace (i.e., $\propto S^{-1/4}$) than we would expect in nearly adiabatic conditions ($\propto S^{-1}$).

5. CONCLUSIONS

Our two-dimensional simulations have revealed that penetrative convection is able to establish a well-mixed region to a depth Δ into the lower stable layer, with that extent of penetration varying either as $\Delta \propto S^{-1}$ or as $\Delta \propto S^{-1/4}$ in terms of the relative stability S of the two layers. As Figure 12 and our scaling analysis in § 4 show, the $S^{-1/4}$ variation prevails at large S (when the lower layer is sufficiently stable in stratification to be able to rapidly decelerate the downward penetrating plumes), with the subsequent thermal boundary layer of thickness l_T (in which the local Peclet number is below unity) yielding the dominant variation of Δ with S. At smaller S it is that first region of nearly adiabatic penetration, of thickness l_P, which is the primary contributor to Δ, and this yields the S^{-1} variation. In all the cases studied here, the Rayleigh numbers $\hat{R}$ characteristic of the unstable layer are sufficiently large that we have explored strongly nonlinear compressible convection in which localized downflow plumes are the dominant structures.

Yet we have sampled only a small region in parameter space, and not only should larger ranges in S be studied, but we also recognize that penetrative convection under far more inviscid conditions or thus higher Reynolds numbers deserves to be explored, for this may admit shear instabilities of the plume flows that can modify their entrainment characteristics and thus possibly also their extent of penetration. Indeed, Porter & Woodward (1993b) have used the piecewise-parabolic method (PPM) code, which is formally inviscid but for some numerical vorticity diffusion, to examine a close relative to the $S = 3$ example in HTM. They find a comparable average extent of penetration Δ, but their two-dimensional solutions at very high spatial resolution also exhibit occasional vortex pairs of

opposite polarity that are able to wander and migrate with little hindrance from the stable stratification (cf. Porter et al. 1991), for the viscous diffusion of vorticity (serving to spin them down) is slow compared to their rapid thermal equilibration in the stable region possessing a large thermal conductivity κ. In other words, the Peclet number of the typical vortex pair is much less than unity, whereas its Reynolds number is large. Though these results are novel, such parameters are unlikely to be achieved in most stellar conditions such as at the base of the solar convection zone, where both the Peclet and Reynolds numbers are expected to be very large. The vortex pairs are like episodic thermals, and might survive in three dimensions as discrete vortex rings, and either is quite different from the long-lived plumes obtained in our simulations. The existence of such plumes may be aided by parameters which yield more comparable vorticity and thermal diffusion times, for the Prandtl number σ_3 in the stable layer in our cases ranges from 2/3 (for $S = 1$) to 1/5 (for $S = 15$), whereas σ_2 in the unstable layer has a value of unity.

We have to be somewhat cautious about these penetration estimates based on two-dimensional flows that are intricate but not turbulent. We expect that the vortex stretching mechanisms which are admitted in three-dimensional settings could destabilize our downflowing plumes, with shearing instabilities modifying entrainment into those downflows. Such turbulent entrainment is unlikely to destroy the plumes but may modify their detailed dynamics. Further, the topology of downflows is likely to change from downflow sheets to discrete plumes with depth, judging from results of the three-dimensional simulations discussed earlier, and this may have an impact on the penetration depth Δ that is achieved. Considerable exploration is needed in the parameter space of three-dimensional penetrative convection, and that work should be extended to deal with thermal conductivities that are explicit functions of temperature and density, thereby modeling stellar settings somewhat more faithfully. The use of direct simulations to study compressible penetrative convection as may be realized in stars is still at an early stage, yet it is a subject that is beginning to receive detailed attention, for as Zahn (1991) has discussed, issues of such mixing have many implications for our understanding of stellar structure and evolution theory.

We wish to thank A. Brandenburg, F. Cattaneo, K. Chan, D. Moore, Å. Nordlund, D. Porter, N. Weiss, and P. Woodward for useful discussions. The computations were performed at the National Center for Atmospheric Research and at the John von Neuman National Supercomputer Center, both supported by the National Science Foundation. This work was supported in part by the National Aeronautics and Space Administration through grants NAGW-2980 and NSG-7611 and contract NAS-5-30386 and by the National Science Foundation through grant ECS-9217394 to the University of Colorado, by the Air Force Office of Scientific Research through grant AFOSR 89-0012 to Columbia University, by the Centre National de la Recherche Scientifique through grant GDR-131, and by Lockheed Independent Research Funds.

REFERENCES

Bogdan, T. J., Cattaneo, F., & Malagoli, A. 1993, ApJ, 407, 316
Cattaneo, F., Brummell, N. H., Toomre, J., Malagoli, A., & Hurlburt, N. E. 1991, ApJ, 370, 282
Cattaneo, F., Hurlburt, N. E., & Toomre, J. 1989, in Solar and Stellar Granulation, ed. R. J. Rutten & G. Severino (Dordrecht: Kluwer), 415
———. 1990, ApJ, 349, L63
Cattaneo, F., & Malagoli, A. 1993, in preparation
Chan, K. L., & Sofia, S. 1986, ApJ, 307, 222
———. 1989, ApJ, 336, 1022
Glatzmaier, G. A., & Gilman, P. A. 1981, ApJS, 47, 103
Graham, E. 1975, J. Fluid Mech., 70, 689
———. 1977 in IAU Colloq. 38, Lec. Notes Phys., 41, Problems of Stellar Convection, ed. E. A. Spiegel & J.-P. Zahn (Berlin: Springer-Verlag), 151
Hossain, M., & Mullan, D. J. 1990, ApJ, 354, L33
———. 1991, ApJ, 380, 631
Hurlburt, N. E. 1983, Ph.D. thesis, University of Colorado, Boulder
Hurlburt, N. E., Toomre, J., & Massaguer, J. M. 1984, ApJ, 282, 557
———. 1986, ApJ, 311, 563 (HTM)
Latour, J., Spiegel, E. A., Toomre, J., & Zahn, J.-P. 1976, ApJ, 207, 233
Latour, J., Toomre, J., & Zahn, J.-P. 1981, ApJ, 248, 1081
Malagoli, A., Cattaneo, F., & Brummell, N. H. 1990, ApJ, 361, L33
Massaguer, J. M., Latour, J., Toomre, J., & Zahn, J.-P. 1984, A&A, 140, 1
Massaguer, J. M., & Zahn, J.-P. 1980, A&A, 87, 315
Nelson, G. D. 1980, ApJ, 238, 659
Nordlund, Å. 1982, A&A, 107, 1
———. 1984, in Small-Scale Dynamical Processes in Quiet Stellar Atmospheres, ed. S. L. Keil (Sunspot: National Solar Obs.), 181
———. 1985, in Theoretical Problems in High-Resolution Solar Physics, ed. H. U. Schmitt (Munich: Max-Planck-Institut für Astrophysik), 1
Nordlund, Å., & Stein, R. F. 1990, Comput. Phys. Comm., 59, 119
Porter, D., & Woodward, P. 1993a, ApJS, submitted
———. 1993b, in preparation
Porter, D., Woodward, P., & Mei, Q. 1991, Video J. Eng. Res., 1, 1
Porter, D., Woodward, P., Yang, W., & Mei, Q. 1990, in Ann. NY Acad. Sci. No. 617, Nonlinear Astrophysical Fluid Dynamics, ed. R. Buchler & S. T. Gottesman, 617, 234
Rast, M., Nordlund, Å., Stein, R. F., & Toomre, J. 1993, ApJ, 408, L53
Rast, M., & Toomre, J. 1993a, ApJ, 419, 224
———. 1993b, ApJ, 419, 240
Renzini, A. 1987, A&A, 188, 49
Roxburgh, I. W., & Simmons, J. 1993, A&A, 277, 93
Schmitt, J. H. M. M., Rosner, R., & Bohn, H. U. 1984, ApJ, 282, 316
Sofia, S., & Chan, K. L. 1984, ApJ, 282, 550
Stein, R. F., & Nordlund, Å. 1989, ApJ, 342, L95
———. 1991, in Lec. Notes Phys., 388, Challenges to Theories of the Structure of Moderate-Mass Stars, ed. D. O. Gough & J. Toomre (Berlin: Springer-Verlag), 141
Toomre, J. 1980, Highlights Astron., 5, 571
Toomre, J., Brummell, N. H., Cattaneo, F., & Hurlburt, N. E. 1990, Comput. Phys. Comm., 59, 105
Toomre, J., Hurlburt, N. E., & Massaguer, J. M. 1984 in Small-Scale Dynamical Processes in Quiet Stellar Atmospheres, ed. S. L. Keil (Sunspot: National Solar Obs.), 222
Toomre, J., Zahn, J.-P., Latour, J., & Spiegel, E. A. 1976, ApJ, 207, 545
Xie, X., & Toomre, J. 1991, in Lec. Notes Phys., 388, Challenges to Theories of the Structure of Moderate-Mass Stars, ed. D. O. Gough & J. Toomre (Berlin: Springer-Verlag), 171
———. 1993, ApJ, 405, 747
Yamaguchi, A. 1984, PASJ, 36, 613
———. 1985, PASJ, 37, 735
Zahn, J.-P. 1991, A&A, 252, 179
Zahn, J.-P., Toomre, J., & Latour, J. 1982, Geophys. Astrophys. Fluid Dyn., 22, 159